ACS OMEGA

http://pubs.acs.org/journal/acsodf

Article

Adsorption of Li(I) Ions through New High-Performance Electrospun PAN/Kaolin Nanofibers: A Combined Experimental and Theoretical Calculation

Tao Ding, Mianping Zheng,* and Yuhan Lin*

Cite This: *ACS Omega* 2022, 7, 11430−11439

Read Online

ACCESS | Metrics & More | Article Recommendations | Supporting Information

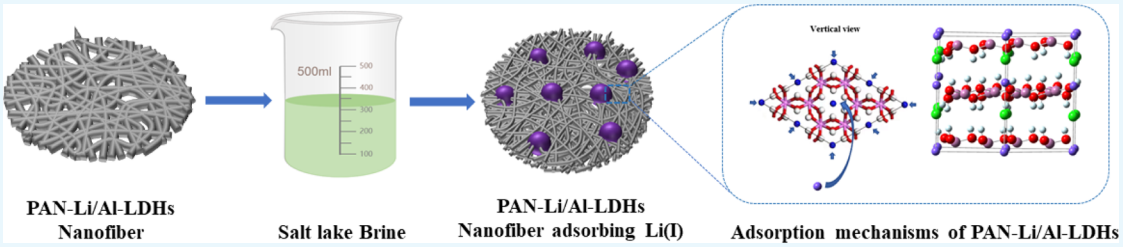

ABSTRACT: Lithium (Li), as a strategic energy source in the 21st century, has a wide range of application prospects. As the demand for lithium resources grows, refining lithium resources becomes increasingly important. A novel method was proposed to directly prepare polyacrylonitrile−LiCl·2Al(OH)$_3$·nH$_2$O (PAN−Li/Al-LDH) composites from kaolin with simple operation and low cost, showing effective adsorption performance for the removal of Li(I) from brine in a salt lake. Moreover, several techniques have been applied for characterization, including X-ray diffraction, Fourier transform infrared spectroscopy, scanning electron microscopy, X-ray photoelectron spectroscopy, and the Brunauer−Emmett−Teller method. Batch adsorption experiments were conducted to investigate the adsorption behaviors of PAN−Li/Al-LDHs for Li(I) in salt-lake brines, indicating that the adsorption equilibrium could reach within 2 h, and the adsorption kinetics for Li(I) conforms to the pseudo-second-order model. The adsorption isotherms are consistent with those obtained by the Langmuir model, with a maximum adsorption capacity of 5.2 mg/g. The competitive experimental results indicated that PAN−Li/Al-LDHs exhibited specific selectivity for Li(I) in the mixed solutions of Mg(II), Na(I), K(I), and Ca(II) with the selectivity coefficients of 9.57, 19.38, 43.40, and 33.05, respectively. Moreover, the PAN−Li/Al-LDHs could be reused 60 times with basically unchanged adsorption capacity, showing excellent stability and regeneration ability. Therefore, PAN−Li/Al-LDHs would have promising industrial application potential for the adsorption and recovery of Li(I) from salt-lake brines.

1. INTRODUCTION

As the lightest alkali metal, lithium (Li) is an important strategic energy source in the 21st century,[1,2] becoming a crucial material in the production of glass,[3,4] nuclear reactors,[5] and lithium batteries.[6−8] In recent years, due to the rapid development of new energy vehicles,[9] the market price of lithium has risen rapidly, and the demand for lithium resources has continued to rise at an annual rate of 10%.[10] Since about 70% of lithium's world resources exist in salt lakes,[11] the selective extraction of Li(I) from salt-lake brines is of great significance for alleviating the tight supply and rising demand for lithium resources in the current market.

Currently, several techniques are available for Li(I) extraction from salt-lake brines, such as precipitation,[12] extraction,[13,14] membrane separation and coupling,[15] salt-gradient solar ponds,[16,17] and adsorption methods.[18] Nowadays, the adsorption method is one of the promising techniques to extract Li(I) from salt lakes, owing to the advantages of high efficiency,[19] simplicity of operation, and low energy consumption.[20] Chitrakar *et al.* prepared the $H_{1.6}Mn_{1.6}O_4$ powder using the hydrothermal method. The adsorption capacity of the powder could reach 40 mg/g within 48 h, and the dissolution-loss rate of Mn was 7.1% after two cycles.[21] Zhang *et al.* prepared HMn_2O_4 particles with an average diameter of 20 nm and an adsorption capacity of 20 mg/g in LiCl solution at pH 10.1, which could selectively adsorb Li(I) in salt lakes with the distribution coefficient K_d of Li(I) as 16,770.63.[22] In order to improve the stability of $H_{1.6}Mn_{1.6}O_4$, Zhang *et al.* calcined $Li_{1.6}Mn_{1.6}O_4$ precursors twice at 450 °C *via* a solid sintering technique to maintain the adsorption capacity at 25 mg/g, with a loss rate of Mn of less

Received: February 1, 2022
Accepted: March 15, 2022
Published: March 22, 2022

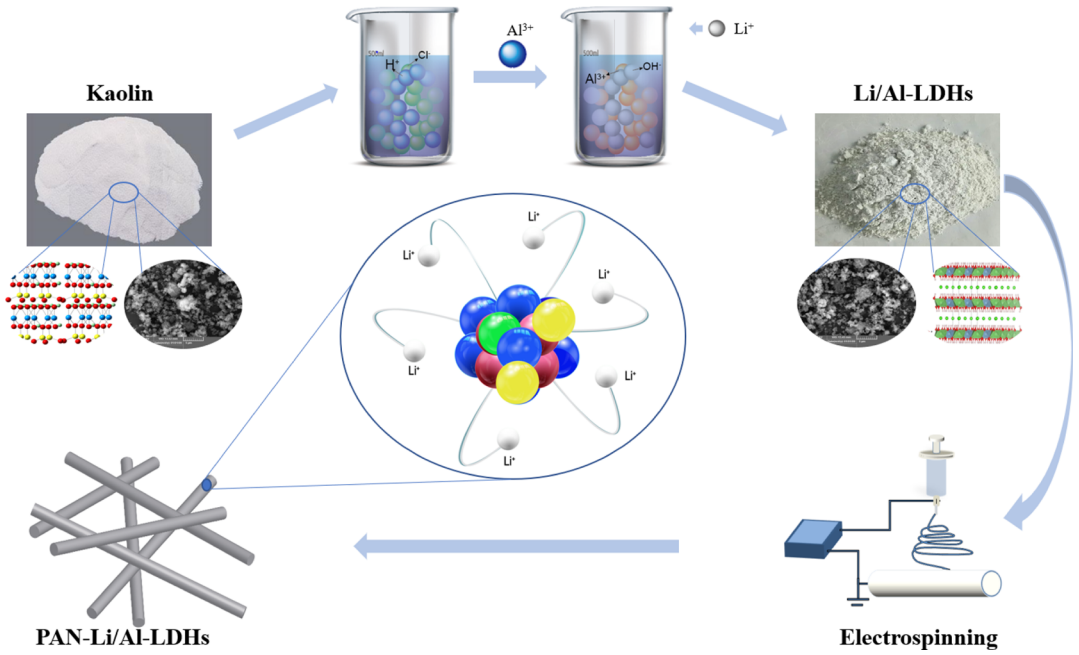

Figure 1. Schematic description of the preparation process of PAN−Li/Al-LDH composite adsorbents.

than 20% after six cycles.[23] In addition, the adsorption of Li(I) under acidic conditions at pH 6.5 was achieved by the adsorbents with introducing TiO_2 into a layered H_2TiO_3 powder, which exhibited a maximum adsorption capacity of 57.8 mg/g at 60 °C, a reduced adsorption time of 8 h, and an adsorption capacity of 25−30 mg/g after six cycles.[24,25] Polymethyl methacrylate was applied as the template to synthesize a Li(I)-ionic sieve precursor and porous nanoscale $Li_4Ti_5O_{12}$ with a saturation adsorption capacity up to 56.81 mg/g.[26] Furthermore, the $LiCl{\cdot}2Al(OH)_3{\cdot}nH_2O$ (Li/Al-LDHs) powder was synthesized using aluminum (Al) compounds, such as $Al(OH)_3$ and $AlCl_3$, and organic polymer as adhesives,[27−29] such as polyvinyl chloride, polyvinylidene fluoride, polystyrene sulfonate, and polyvinyl alcohol (PVA).[30−34] The adsorption capacity of Li/Al-LDHs after granulation reached 1 to 5 mg/g and Li(I) could be directly eluted with deionized water.[35,36] Although several strategies have been attempted to improve the adsorption capacity, stability, and selectivity of the adsorbent for Li(I), these adsorbents are powdery or granular in nature and have significant resistance to flow during the dynamic adsorption process. Moreover, the separation of these adsorbents is commonly difficult due to their agglomeration, which hinders the practical industrial application of adsorbents. Therefore, it is necessary and urgent to develop adsorbents for Li(I) recovery with low flow resistance and easy separation.

With the advantages of low flow resistance, large specific surface area, and easy separation, fiber-based adsorbents are widely used for metal recovery in solution. Li *et al.* conducted the sol−gel polymerization of 3-mercaptotrimethoxysilane on electrospun polyacrylonitrile (PAN) nanofibers and synthesized new sulfhydryl-functionalized silica nanofibers. The adsorption of Hg(II) reached saturation within 30 min with a maximum adsorption capacity of 57.49 mg/g.[37] To obtain more adsorption sites, oxosilane derived from tannic acid (polyphenol)-induced biomimetic co-deposition of cardanol was grafted onto a cellulose nanofiber framework to adsorb Cu(II) from wastewater with a saturated adsorption capacity of 45.6 mg/L.[38] Jamshidifard *et al.* prepared PAN/chitosan nanofibers containing UiO-66-NH_2MOF, having a specific surface area of 1118 m^2/g according to the Brunauer−Emmett−Teller (BET) method, and an inner pore diameter ranging from 9 to 13 Å. The maximum adsorption capacities of these adsorbents were 441.2, 415.6, and 372.6 mg/g for Pb(II), Cd(II), and Cr(VI), respectively, indicating excellent separation effects of such composite fibers.[39] Koushkbaghi *et al.* added aminated Fe_3O_4 nanoparticles to polyethersulfone/PVA nanofibers and then synthesized bilayer mixed matrix membranes for the removal of Cr(VI) and Pb(II) from water. The maximum adsorption capacities of Cr(VI) and Pb(II) were 509.7 and 525.8 mg/g, respectively, and the adsorption capacity of the adsorbents remained basically unchanged after three adsorption cycles.[40] The above-reported studies suggest that the fiber-based adsorbents with stable structure have promising application prospects. To the best of our knowledge, very little research has been devoted towards fiber-based adsorbents for the selective separation of Li(I) from salt lakes.

In this work, a high-performance adsorbent material for the selective separation and recovery of Li(I) from salt-lake brines was designed and synthesized through the combination of electrospinning technique and Li/Al-LDHs prepared from kaolin. Specifically, kaolin-prepared Li/Al-LDHs bulk phases were blended into electrospun nanofibers to synthesize a novel adsorbent material with high stability, low cost, and excellent hydrodynamic properties. The internal structure, stability, and mechanisms of directional capture of the adsorbent Li(I) were revealed according to a series of characterization techniques, adsorption experiments, and theoretical calculations.

2. MATERIALS AND METHODS

2.1. Materials and Chemicals. The chemical reagents (analytical grade) were mainly purchased from Sinopharm Chemical Reagent Co., Ltd. and Rhawn Reagent Co., Ltd. [Supporting Information (Text S1)]. The brine was sourced from Zabuye Salt Lake in the Tibet Autonomous Region,

https://doi.org/10.1021/acsomega.2c00658
ACS Omega 2022, 7, 11430−11439

China. The pH of the brine was 7.5, and the elemental concentrations were determined using inductively coupled plasma-atomic emission spectroscopy (ICP-AES), as shown in the Supporting Information (Table S1).

2.2. Li/Al-LDH Nanofibers Synthesized from Kaolin. 5 g of kaolin, as raw material, was placed in a muffle furnace to be activated at 700 °C for 1 h. The activated kaolin was dissolved with 50 mL of HCl at a concentration of 20 wt %. The solution was stirred at 90 °C for 5 h, and a 50 mL LiCl solution with a concentration of 11.58 g/L was prepared. The above kaolin solution and LiCl solution were simultaneously added to 2 mol/L NaOH solution. The pH value was downregulated to a final value of 4.5 using a blender (75 °C, 150 rpm). After continuous stirring and aging for 30 min, the reactants were filtered and dried at 100 °C for 2 h, and the products were mechanically ground to form nanoparticles. The product obtained in this step was the Li/Al-LDH nanosized powder.

The pretreated 0.5 g Li/Al-LDH nanosized powder was added to *N*,*N*-dimethylformamide for 30 min of ultrasonic dispersion, and then PAN fibers were added. The uniform and transparent spinning solution, with a concentration of 13 wt %, was prepared by magnetic stirring at 90 °C for 4 h. The spinning solution was poured into a 10 mL needle syringe with an 18 G needle as the spinning head, having an inner diameter of 0.83 mm. Then, the syringe was installed on a micropump to control the flow rate of the spinning solution. The following specific parameters were used for the spinning process: a voltage of 15 kV and a spinning solution flow rate of 0.25 mL/min. The drum receiver was rotated at 450 rpm with a receiving distance of 150 mm. PAN−Li/Al-LDH nanofibers can be prepared by vacuum drying the spinning products in an oven at 50 °C for 12 h (Figure 1).

2.3. Characterization. The as-synthesized experimental samples were characterized by using X-ray diffraction (XRD), scanning electron microscopy (SEM), BET, X-ray photoelectron spectroscopy (XPS), and Fourier transform infrared (FT-IR) spectroscopy. The concentrations of ions in the brine solution were determined using ICP-AES. Detailed information related to the characterization can be found in the Supporting Information (Text S2).

2.4. Adsorption Experiment. A static adsorption experiment of Li(I) was conducted in the batch mode to investigate the adsorption kinetics, adsorption isotherms, and adsorption selectivity of Li(I), as well as the adsorption capacity under different pH values. In addition, the recycling performance was studied using a stationary bed. The adsorption kinetic data were analyzed using the pseudo-first-order and pseudo-second-order models. The adsorption isotherm data were fitted using the Langmuir and Freundlich models. The reusability of PAN−Li/Al-LDH nanofibers was further investigated by Li(I) desorption with the stationary bed adsorption method. A series of experiments were carried out to investigate the selective adsorption of ionic materials in salt-lake brines. More detailed information is provided in the Supporting Information (Text S3).

2.5. Calculation Methods. The adsorption energy of Li(I) on PAN−Li/Al-LDHs and the structural energy differences of Al, O, Li, Cl, and H compounds were calculated using the generalized gradient approximation of Perdew−Burke−Ernzerhof (GGA-PBE).[41−43] The structural energy differences of Al, O, Li, Cl, and H were calculated, respectively.[44,45] Additional details are provided in the Supporting Information (Text S4).

3. RESULTS AND DISCUSSION

3.1. Characterization of PAN−Li/Al-LDH Composite Adsorbents. Figure 2 shows the XRD patterns of Li/Al-LDHs prepared from kaolin. The XRD pattern of kaolin exhibited shallow and symmetrical peaks, including the characteristic peaks of the Si−O structure at a 2θ of 26° and the characteristic peaks of Al−O at 42 and 46°.[46] No distinct impurity peak was found in the spectrum of kaolin. However, the XRD pattern of Li/Al-LDHs prepared from kaolin shows sharp peaks, indicating excellent crystallinity. The peaks at 2θ values of 11.42 and 23.19° indicated the typical crystal form of Li/Al-LDHs, confirming the preparation of Li/Al-LDHs based on kaolin.[47,48] Figure 3 displays SEM images of PAN−Li/Al-LDHs before and after adsorption of Li(I). As can be seen from Figure 3a, the nanofibers were regular and uniformly distributed with a diameter of about 300 nm. The surface of the nanofibers was smooth, with abundant pores distributing between the fibers. These characteristics of PAN−Li/Al-LDHs would be conducive for the capture of the target ions from the salt-lake brine.

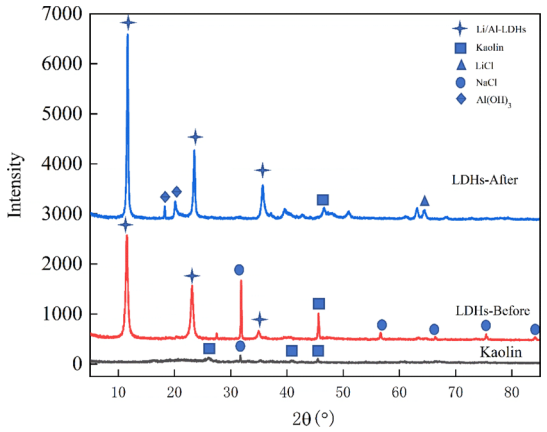

Figure 2. XRD patterns of Li/Al-LDH composite adsorbents prepared from kaolin before and after adsorption.

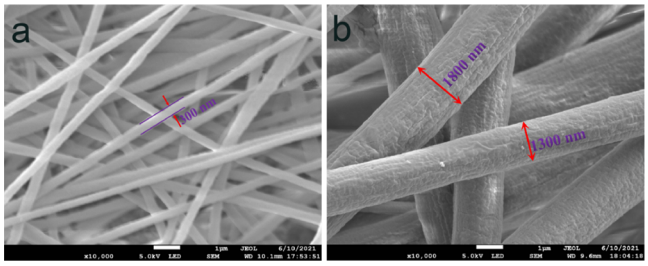

Figure 3. SEM images of PAN−Li/Al-LDH composite adsorbents (a) before and (b) after adsorption of Li(I).

Figure 4 presents the nitrogen (N_2) adsorption isotherms of Li/Al-LDHs. As shown in Figure 4a, there is a type IV adsorption isotherm before adsorption, accompanied by hysteresis loops after condensation.[49] This indicated that the as-prepared Li/Al-LDHs were mesoporous adsorbents, and the cylindrical pores were mainly manifested in the structure with uniform pore distribution.[50] According to the IUPAC classification, the hysteresis possibly resulted from the capillary

https://doi.org/10.1021/acsomega.2c00658
ACS Omega 2022, 7, 11430−11439

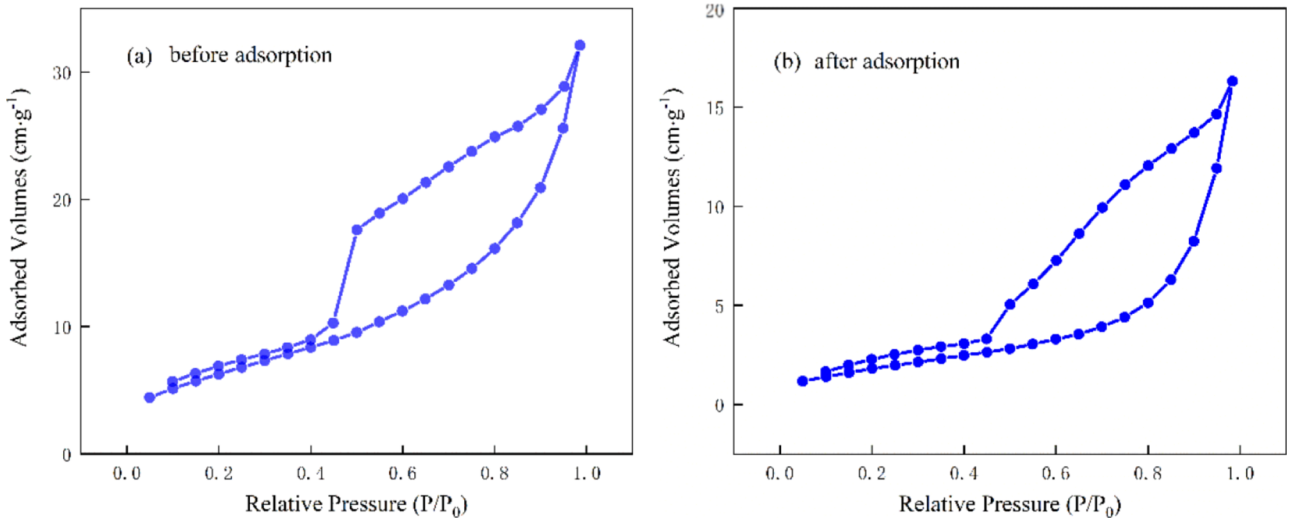

Figure 4. N_2 adsorption and desorption isotherms of Li/Al-LDH composite adsorbents (a) before and (b) after adsorption of Li(I).

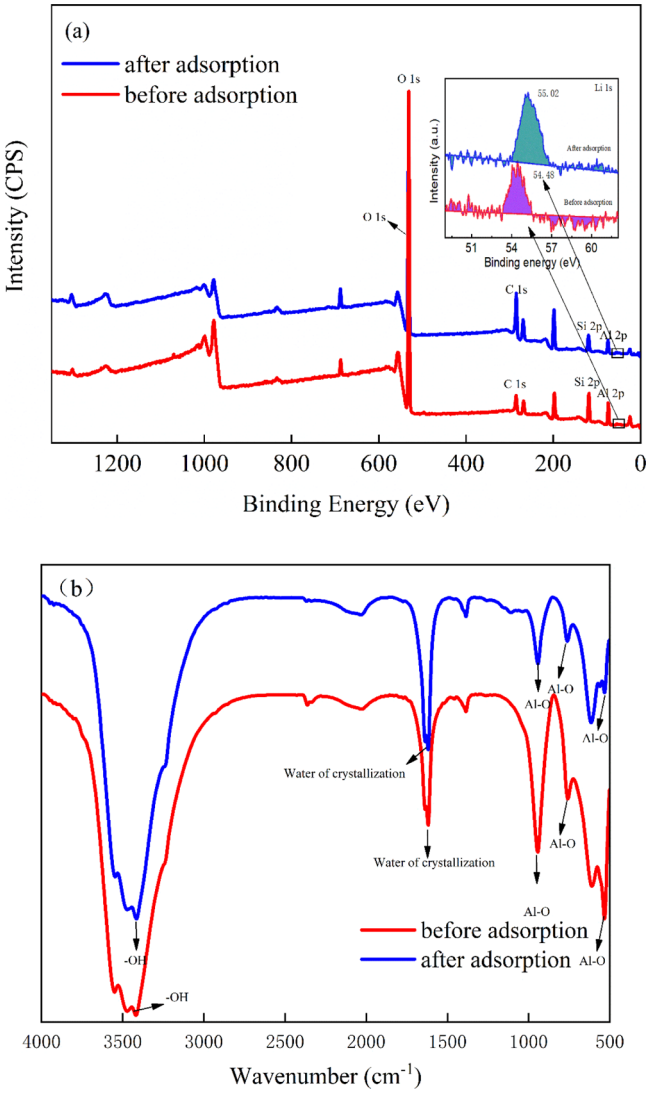

Figure 5. XPS fitting (a) and the FT-IR spectra (b) of Li/Al-LDH composite adsorbents before and after adsorption of Li(I).

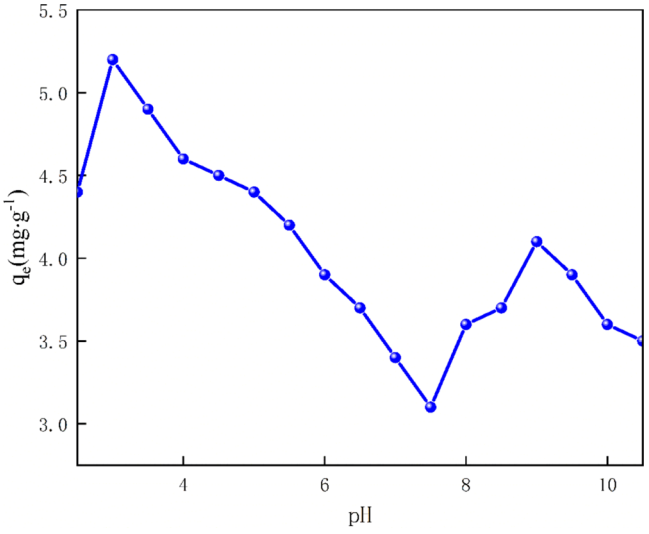

Figure 6. Influences of the pH value on the adsorption capacity of PAN−Li/Al-LDHs for Li(I).

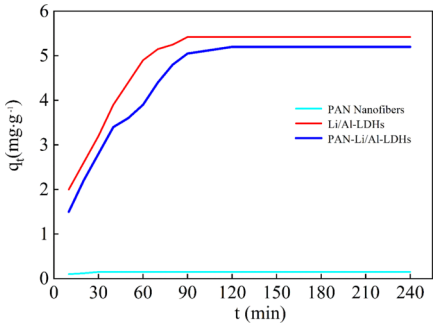

Figure 7. Change in the adsorption capacity with time.

condensation of the mesopores, revealing abundant intermediate pores and well-developed pore structure in the Li/Al-LDHs. As the pressure increased with $P{\cdot}P_0^{-1} < 0.8$, the adsorption capacity increased slowly with a small slope of the adsorption curve, indicating the existence of certain micropores in the Li/Al-LDHs. While as the pressure increased with $0.8 < P{\cdot}P_0^{-1} < 1$, the slope of the adsorption curve increased rapidly, suggesting the large number of mesoporous in the adsorbents.[51] As can be seen from Figure 4b, a type IV

https://doi.org/10.1021/acsomega.2c00658
ACS Omega 2022, 7, 11430−11439

Table 1. Comparison on Li(I) Adsorption Performance of Adsorbents in the Reported Literature

sorbents	adsorption equilibrium time (h)	adsorption capacity (mg/g)	refs
PAN−Li/Al-LDHs	2	5.2	current research
Li/Al-LDHs	10	3.0	36
MLDHs	4−5	3.46	48
Li/Al-LDHs@PVCM	10	4.92	58

isotherm was displayed with a decreased maximum N_2 adsorption capacity and a change in the hysteresis loops, indicating the varied pore diameter and pore volume after adsorption. The adsorption curve increased slowly with increasing pressure under $P{\cdot}P_0^{-1}$ below 0.8, while it increased rapidly with increasing pressure under $P{\cdot}P_0^{-1}$ above 0.6. The above results indicated that the Li/Al-LDHs displayed a decreased pore volume after adsorption and presented a typical type IV adsorption isotherm before and after adsorption, which confirmed the uniform pore distribution and stable structure of the adsorbents.[52,53]

Figure 5a shows XPS characterization of Li/Al-LDHs. It can be seen that Al, O, and Li elements appeared in the Li/Al-LDHs with binding energies of 73.68, 531.28, and 54.48 eV, respectively.[54−56] Figure 5b displays the FT-IR spectra of Li/Al-LDHs before and after the adsorption of Li(I). Before the adsorption, the FT-IR spectra of Li/Al-LDHs exhibited Al−O stretching vibration peaks at 935, 753, and 519 cm^{-1}. The infrared band near 3450 cm^{-1} was attributed to the stretching vibration of OH groups, and the infrared band at 1622 cm^{-1} was ascribed to the adsorbed water bending vibrations. The absorption of Li(I) in the Li/Al-LDHs led to the Al−O stretching vibration peak at 1004 cm^{-1}, and the changes at 3622 and 3566 cm^{-1}, which were attributed to the stretching vibration of OH groups in the Li/Al-LDHs, are consistent with the results in the reported studies.[55,57,58]

3.2. Effect of pH on Adsorption. The pH value is a crucial parameter influencing the adsorption performance of metal ions because it may change the surface charge distribution of adsorbents and the morphology of metal ions in an aqueous solution.[59] The pH values ranging from 2.5 to 10.5 were investigated for the adsorption capacity for Li(I) since the adsorbed material would be dissolved under the pH value below 2.5, and other metal ions existing in the aqueous solution would precipitate out with OH^- under the pH value above 10.5.[60] As can be seen from Figure 6, the adsorption capacity for Li(I) reached a maximum value of 5.2 mg/g at pH 3.0. As the pH value increased to 7.5, the adsorption capacity for Li(I) decreased. During the adsorption process, Li(I), anions, and water molecules firstly entered the layers of adsorbents. Owing to the presence of a large amount of Al(III) on the layer walls of adsorbents, most of the OH^- in the system could combine with Al(III) to form an Al−OH structure; however, H^+ was readily mobilized at a low pH value. In this case, Li(I) could bind to Al−O− to enter the

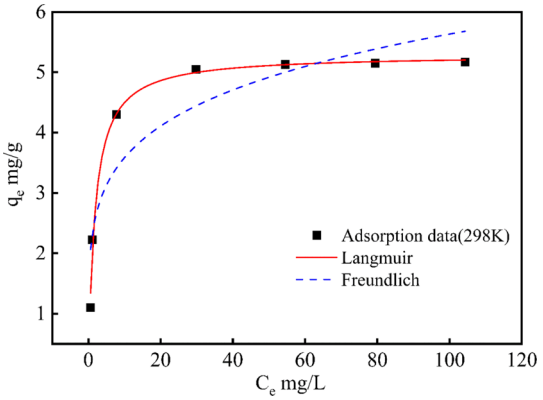

Figure 8. Comparison of Langmuir and Freundlich adsorption models for Li(I) adsorption of the adsorbing materials.

nodes in the layers of adsorbents. With the increase of the pH value, the increased concentration of OH^- in the system made it more difficult for H^+ to be free, which hindered the binding between Li(I) and Al−O. The adsorption of Li(I) increased at the pH value of 7.5−9.0, which might be because Al(III) on the layer surface of adsorbent materials could bind partially with Li(I) in the form of $[Li(OH)_2]^-$ in addition to OH^- in the system. The adsorption capacity for Li(I) decreased slightly as the pH value in the system increased further to 10.5 due to the partial transformation of Al(III) to AlO_2^- in the adsorbents. In this case, Li(I) mainly existed in the form of complex OH^- states with a small amount of free Li(I). The capture of Li(I) adsorbents was more likely to depend on the binding of AlO_2^- and Li(I). Excess OH^- would compete with the AlO_2^- structure in the adsorbent material, resulting in a decrease in the adsorption capacity.

3.3. Adsorption Behaviors. The adsorption of Li(I) by the adsorbents as a function of time is shown in Figure 7. The adsorbents exhibited a fast adsorption for Li(I), with over 95% of adsorption rate at around 90 min and the equilibrium within 2 h. Compared with similar adsorbents reported in the literature, the PAN−Li/Al-LDHs in this work presented a superior adsorption performance for Li(I), as listed in Table 1.

The excellent adsorption performance of PAN−Li/Al-LDHs was mainly attributed to the formation of the Al−O structure with a large amount of OH^- binding to Al(III) in the adsorbents. The decreased adsorption rate in the later stages might be due to the slowing down of the Li(I) diffusion with the binding of Al−O in the $Al(OH)_3$ layers. During the preparation of the adsorbent, the imported Li(I) was removed by water washing, resulting in the generation of the vacant sites for Li(I) adsorption. Since these adsorption sites were commonly located deeper in the adsorbents, Li(I) should migrate to the interior by molecular diffusion, and thus a longer time was required to reach the adsorption equilibrium.

In order to reveal the adsorption mechanisms for Li(I), the experimental data were analyzed based on the pseudo-first-order and pseudo-second-order kinetic models. Table 2 lists the relevant kinetic parameters, and the Supporting Informa-

Table 2. Kinetic Parameters

	pseudo-first-order			pseudo-second-order		
temperature (K)	k_1 (min^{-1})	$q_{e,cal}$ (mg/g)	R_1^2	k_2 (mg/(g·min))	$q_{e,cal}$ (mg/g)	R_2^2
298	0.095	4.79	0.924	0.015	5.54	0.967

https://doi.org/10.1021/acsomega.2c00658
ACS Omega 2022, 7, 11430−11439

Table 3. Relevant Parameters of Langmuir and Freundlich Models

		Langmuir			Freundlich		
temperature (K)	$q_{e,exp}$ (mg/g)	$q_{max,cal}$ (mg/g)	K_L (L/mg)	R_L^2	n	K_F (mg/g)	R_F^2
298	5.15	5.29	0.566	0.992	5.094	2.281	0.825

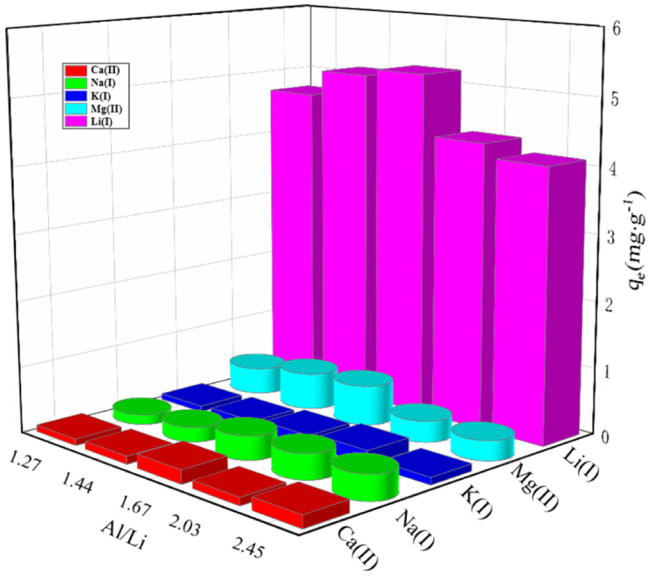

Figure 9. Adsorption of PAN−Li/Al-LDHs for Li (I), Mg(II), K(I), Na(I), and Ca(II) under different ratios of aluminum to lithium.

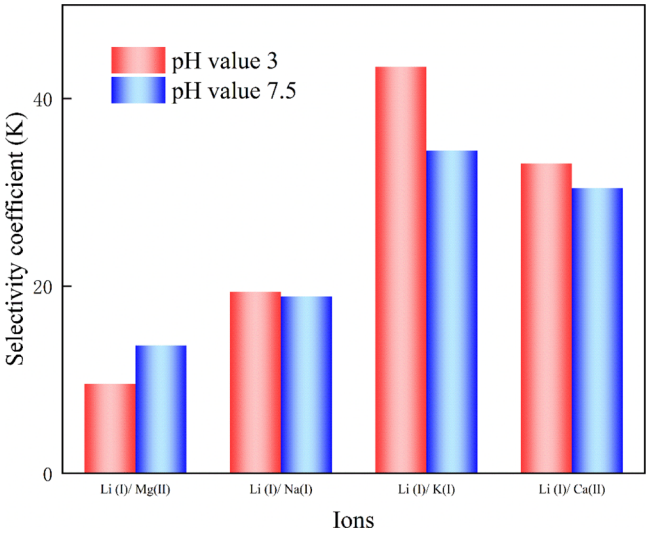

Figure 10. Selectivity of the adsorbing materials for Li(I) at the pH values of 3.0 and 7.5.

tion (Figure S1) shows the fitting curve of the kinetics. According to the kinetic data, the pseudo-second-order kinetics was more appropriate to describe the whole adsorption process with a correlation coefficient of 0.967. Besides, the maximum equilibrium adsorption capacity calculated from the pseudo-second-order kinetics was closer to the experimental data, indicating the chemical process of adsorption. As expected, the presence of Al(III) in the adsorbents allowed binding to OH^-, while the amount of Al(III) determined the quantity of OH^- and ultimately the amount of Li(I). However, during the preparation of the adsorbent, the Li(I) adsorption vacancies were found in the octahedra between the $Al(OH)_3$ layers, and the diffusion of Li(I) between the $Al(OH)_3$ layers is the determining factor for the entire adsorption process. Therefore, the overall adsorption rate could be accelerated by a certain heating or stirring.

Table 4. Adsorption Parameters for Selectivity of the Adsorbent

		distribution coefficient (K_d) (mL/g)		
ions	pH	D (Li)	D (M)	selectivity coefficient (K)
Li(I)/Mg(II)	3.0	116.32	12.15	9.57
	7.5	66.10	4.84	13.65
Li(I)/Na(I)	3.0	140.50	7.25	19.38
	7.5	68.38	3.62	18.89
Li(I)/K(I)	3.0	139.32	3.21	43.40
	7.5	68.83	2.00	34.42
Li(I)/Ca(II)	3.0	139.49	4.22	33.05
	7.5	67.00	2.20	30.45

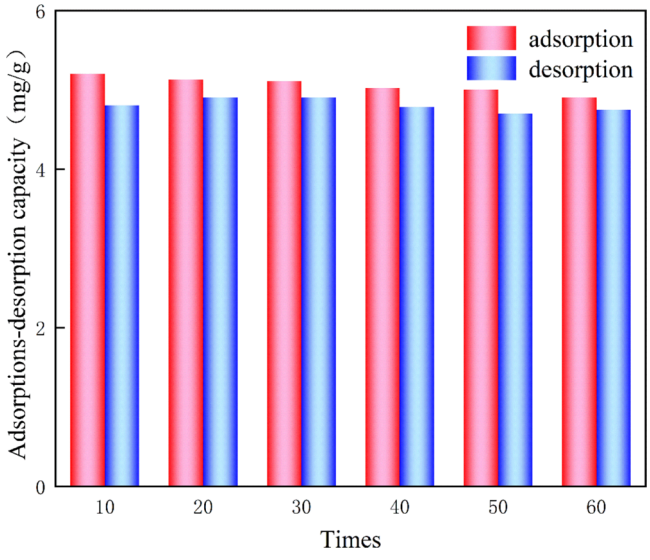

Figure 11. Cyclic capacity.

Figure 8 shows the adsorption isotherms of Li/Al-LDH composite adsorbents for Li(I). It can be seen that the equilibrium adsorption capacity increased with the increase of the initial concentration. As Li(I) concentration in the system increased, the driving force for mass transfer increased. As mentioned above, the adsorption sites for Li(I) in the adsorbents were derived from the diffusion of Li(I) into the octahedra between the $Al(OH)_3$ layers. When these fixed adsorption sites were largely occupied by Li(I), the adsorption capacity would not greatly change. The experimental data were fitted by the Freundlich and Langmuir adsorption isotherm models, and the relevant data are listed in Table 3. It can be found that the correlation coefficient fitted by the Langmuir adsorption isotherm model was closer to 1, and the calculated maximum adsorption capacity was very similar to the experimental adsorption capacity. Therefore, it could be

https://doi.org/10.1021/acsomega.2c00658
ACS Omega 2022, 7, 11430−11439

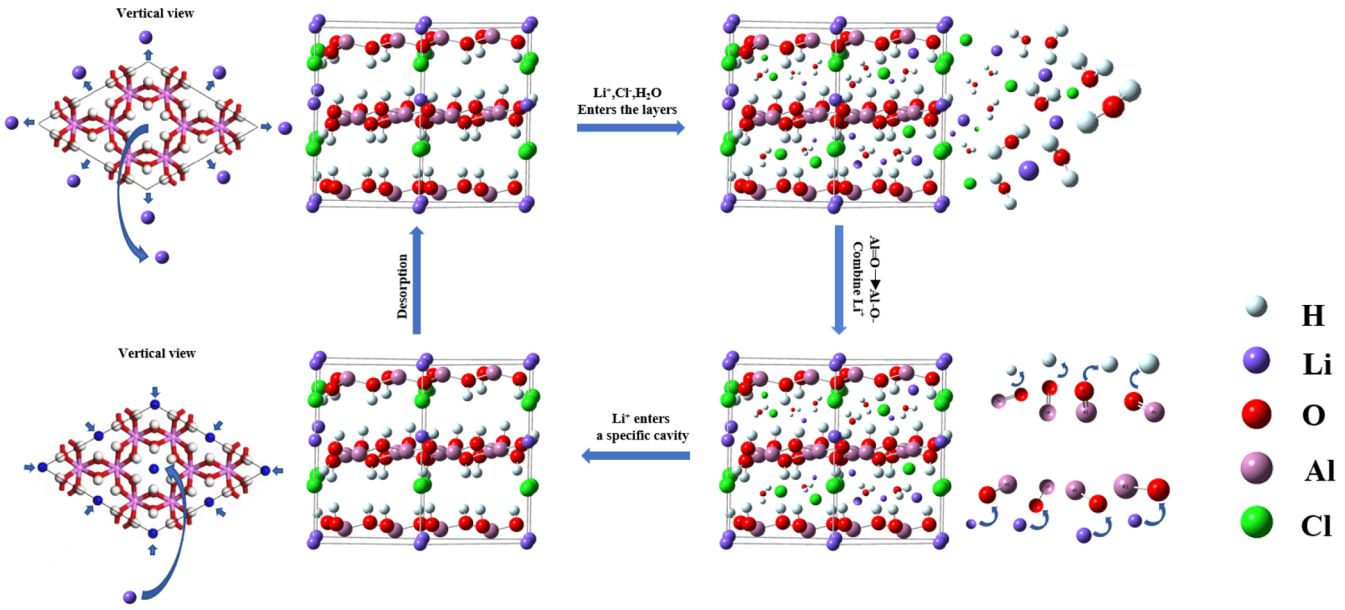

Figure 12. Adsorption mechanisms of PAN−Li/Al-LDHs.

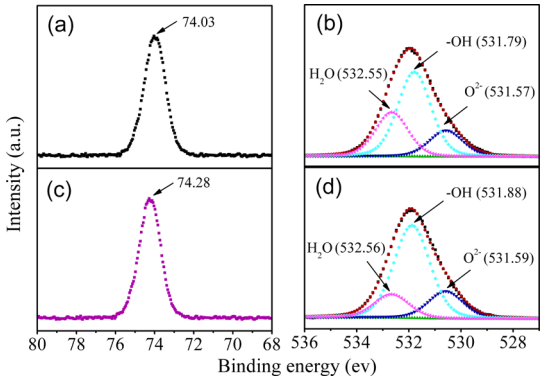

Figure 13. XPS survey spectra (a,b) before and (c,d) after the adsorption of Li(I) by PAN−Li/Al-LDHs.

concluded that the adsorption process was more in agreement with the Langmuir adsorption isotherm model, and the adsorption process could be regarded as monolayer adsorption. During the preparation of the adsorbent, Li(I) was first introduced into the octahedra between the $Al(OH)_3$ layers and then was adsorbed through vacancies generated by water washing. Therefore, the preparation method mainly determined the number of vacancies for Li(I) adsorption, and these adsorbed vacancies existed a certain space between them but no interaction.

3.4. Selectivity and Regeneration. The selectivity to target ions and the regeneration performance of the adsorbents are directly related to the prospects of practical industrial applications. Since Li(I) commonly coexisted with K(I), Na(I), Ca(II), and Mg(II), these ions were chosen as the interfering ions to investigate the selectivity of the adsorbents for Li(I). Figure 9 presents the comparison of the adsorption capacities of the adsorbents prepared with different Al−Li ratios. Table 3 lists the relevant selectivity parameters. It can be seen that the adsorbents displayed an obviously higher adsorption capacity for Li(I) that other metal ions in the mixed solution. In addition, the adsorption capacity for Li(I) increased with the increase of the Al−Li ratio from 1.27 to 1.67 and then decreased. During the adsorbent preparation, the increase of Al(III) allowed more OH^- binding to the layer walls and generated more Al−O− structures from free H^+ under acidic conditions, contributing to a large amount of adsorbed Li(I). The high concentration of Li(I) was conducive to the diffusion toward the octahedra between the $Al(OH)_3$ layers. When the Al−Li ratio reached a certain value, the adsorption capacity for Li(I) decreased, probably due to the formation of fewer vacancies for Li(I) adsorption in the octahedra between the $Al(OH)_3$ layers. Thus, the excellent selectivity for Li(I) was probably because of the good match of Li(I) within adsorption vacancies in the adsorbents. In contrast, the adsorbents had a certain affinity for Mg(II) due to the similar radius of Mg(II) (0.065 nm) with Li(I) (0.068 nm).

Figure 10 displays the selectivity of the adsorbents for Li(I) at pH values of 3.0 and 7.5, and Table 4 lists the relevant selectivity parameters. It was found that the adsorbents exhibited the highest adsorption capacity and a stronger affinity for Li(I) at pH 3.0. All the metal ions had less adsorption capacity at pH 7.5, mainly because it is more difficult for H^+ in Al−OH to liberate, mobilize, and bind to these metal ions at a higher pH value.

The stability of the adsorbents was detected through eluting the adsorbed Li(I) eluted with deionized water. After 60 adsorption−desorption cycles, the adsorbents still retained the excellent adsorption performance and selectivity for Li(I), as shown in Figure 11. The adsorption capacity could reach 4.9 mg/g, and the selectivity coefficients for Mg(II), Na(I), K(I), and Ca(II) were 9.57, 19.38, 43.40, and 33.05, respectively. These results indicated that the prepared adsorbents displayed excellent stability with broad application prospects.

3.5. Adsorption Mechanisms. The adsorption mechanisms of Li(I) on the surface of nanofibers were explained from a macroscopic perspective through adsorption experiments. In addition, the capture mechanisms of Li(I) adsorption sites were revealed from a microscopic perspective by means of XPS, FT-IR spectroscopy, and theoretical calculations. Figure 12 illustrates a schematic diagram of the relevant adsorption mechanisms. Figure 5b compared the FT-IR spectra of the

https://doi.org/10.1021/acsomega.2c00658
ACS Omega 2022, 7, 11430−11439

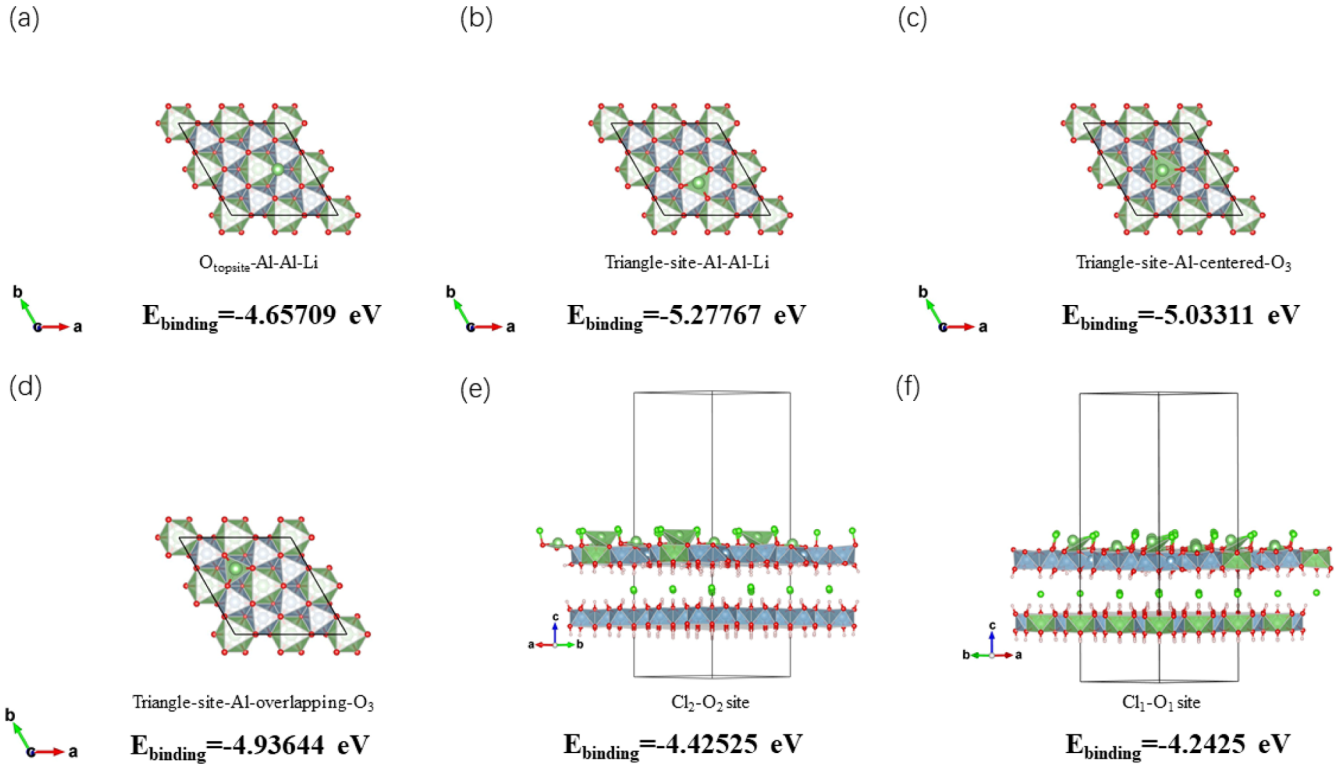

Figure 14. Calculation of adsorption energies at each site (a) $O_{topsite}$-Al−Al−Li (b) triangle-site-Al−Al−Li (c) triangle-site-Al-centered-O_3 (d) triangle-site-Al-centered-O_3 (e) Cl2−O2 site (f) Cl_1−O_1 site.

adsorbent before and after the adsorption of Li(I). Before adsorption, the absorption peaks at 935, 753, 519, and 3450 cm^{-1} corresponded to the Al−O and OH stretching vibrational peaks in Li/Al-LDHs, respectively. After adsorption, the absorption peak at 935 cm^{-1} was shifted to 933 cm^{-1}, and that at 3450 to 3445 cm^{-1} due to the fact that the metal ions required more energy to vibrate after binding. Figure 3b shows the SEM image of the adsorbents after the adsorption of Li(I). It can be seen that the diameter of the nanofibers increased to 1500−2000 nm after adsorption, around 5−7 times thicker than that before adsorption. The surface of the adsorbents became rougher, with a large number of metal ions adsorbed. These changes were mainly due to the increased distance between the $Al(OH)_3$ layers after adsorption of Li(I), which could be proved by the BET results. As listed in the Supporting Information (Table S2), the specific surface area of the adsorbents decreased from 19.342 to 8.709 m^2/g, and the specific pore volume decreased from 0.034 to 0.026 cm^3/g after adsorption. Moreover, the average pore diameter decreased from 3.537 to 1.942 nm. These results demonstrated that Li(I) had entered the adsorption vacancies and was adsorbed by the adsorbents.

Figure 5a shows the chemical composition of the as-adsorbed material before and after the adsorption of Li(I). After adsorption, a clear characteristic peak of the element Li appeared, and the main peak shifted to the left, indicating the adsorption of Li(I). In addition, Figure 13a,b demonstrates the narrow-spectrum fitting of Al and O before adsorption. The characteristic peak at 74.03 eV was attributed to Al−O in $Al(OH)_3$, consistent with the characteristic peak in the standard $Al(OH)_3$.[55,61] However, the narrow-spectrum fitting of Al and O changed distinctly after the adsorption of Li(I), with the characteristic peak of Al−O increasing to 74.28 eV, and those of −OH, H_2O, and Al−O shifting to the right, which may be due to the O in Al−O participating in the adsorption of Li(I) as an electron donor. Based on the characterization results and literature reports, the main component of Li/Al-LDHs could be confirmed as $LiCl{\cdot}2Al(OH)_3{\cdot}nH_2O$, and the O peak changed in the peak-splitting fitting of XPS. It can be inferred from the structure of the adsorbents that the element O in PAN−Li/Al-LDHs played an important role in the adsorption of Li(I). Figure 14 shows the adsorption energies of the adsorption sites in PAN−Li/Al-LDHs calculated using the GGA-PBE functional. According to the calculated results, the adsorption energies were found on six sites on the layered PAN−Li/Al-LDH structure and had large values for Al−O and Al−Al structures, corresponding to the mechanism derived from the XPS results, that is, the O in Al−O participated in the adsorption of Li(I) as an electron donor.

4. CONCLUSIONS

In this work, PAN−Li/Al-LDH composite adsorbents were directly synthesized using kaolin as raw material, and they displayed efficient and selective adsorption for Li(I) from the salt-lake brine. A series of adsorption experiments indicated that the adsorption kinetics of PAN−Li/Al-LDH adsorbents were in accordance with the pseudo-second-order model, and the isothermal adsorption conformed to the Langmuir model with a maximum adsorption capacity of 5.2 mg/g at pH 3. The adsorption occurred through a chemical adsorption process. The selectivity coefficients of PAN−Li/Al-LDHs were 9.57, 19.38, 43.40, and 33.05 for the mixed solutions of Mg(II), Na(I), K(I), and Ca(II), respectively, indicating the selective adsorption of PAN−Li/Al-LDH adsorbents for Li(I). After 60 adsorption−desorption cycles, the adsorption capacity could be maintained at 4.9 mg/g, suggesting favorable stability and

https://doi.org/10.1021/acsomega.2c00658
ACS Omega 2022, 7, 11430−11439

strong regeneration ability. Therefore, PAN−Li/Al-LDH composite adsorbents could be applied for the separation and recovery of Li from salt-lake brines, making it a novel adsorption material with the potential for industrial applications.

■ ASSOCIATED CONTENT

Supporting Information

The Supporting Information is available free of charge at https://pubs.acs.org/doi/10.1021/acsomega.2c00658.

List of chemicals, characterization, sorption experiments, computational method, adsorption kinetics fitting, elements contents in brine, and surface area and pore size of samples (PDF)

■ AUTHOR INFORMATION

Corresponding Authors

Mianping Zheng − *MNR Key Laboratory of Saline Lake Resources and Environments, Institute of Mineral Resources, Chinese Academy of Geological Sciences, Beijing 100037, China*; Phone: +86 10 6899 2231; Email: zhengmp2010@126.com

Yuhan Lin − *College of Geoscience and Surveying Engineering, China University of Mining and Technology (Beijing), Beijing 100083, China*; Phone: +86 10 6832 7637; Email: 1406973096@qq.com

Author

Tao Ding − *College of Geoscience and Surveying Engineering, China University of Mining and Technology (Beijing), Beijing 100083, China*; orcid.org/0000-0002-2724-7869

Complete contact information is available at: https://pubs.acs.org/10.1021/acsomega.2c00658

Notes

The authors declare no competing financial interest.

■ ACKNOWLEDGMENTS

The authors gratefully thank the National Natural Science Foundation of China for financial support (no. 91962219).

■ REFERENCES

(1) Tarascon, J.-M. Is Lithium the New Gold? *Nat. Chem.* **2010**, *2*, 510.

(2) Liu, X.; Zhong, M.; Chen, X.; Li, J.; He, L.; Zhao, Z. Enriching lithium and separating lithium to magnesium from sulfate type salt lake brine. *Hydrometallurgy* **2020**, *192*, 105247.

(3) Delgado, M. A.; Sánchez, M. C.; Valencia, C.; Franco, J. M.; Gallegos, C. Relationship among microstructure, rheology and processing of a lithium lubricating grease. *Chem. Eng. Res. Des.* **2005**, *83*, 1085−1092.

(4) Blink, J. A.; Hogam, W. J.; Hovingh, J.; Meier, E. R.; Pitts, J. H. *High-Yield Lithium-Injection Fusion-Energy (HYLIFE) reactor*; Lawrence Livermore National Laboratory, 1985.

(5) Tyrsa, V. E.; Burtseva, L. E. Generation of thermonuclear energy by fusing hydrogen and lithium atoms. *Tech. Phys.* **2003**, *48*, 807−812.

(6) Lee, J.; Kitchaev, D. A.; Kwon, D. H.; Lee, C. W.; Papp, J. K. Reversible Mn^{2+}/Mn^{4+} double redox in lithium-excess cathode materials. *Nature* **2018**, *556*, 185−190.

(7) Tian, C.; Wu, J.; Ma, Z.; Li, B.; Zhang, X.; Zu, X.; Xiang, X.; Li, S. A melt-diffusion strategy for tunable sulfur loading on CC@MOS_2 for lithium-sulfur batteries. *Energy Rep.* **2020**, *6*, 172−180.

(8) Zhang, F.; Lou, S.; Li, S.; Wang, J. Surface regulation enables high stability of single-crystal lithium-ion cathodes at high voltage. *Nat. Commun.* **2020**, *11*, 3050.

(9) Martin, G.; Rentsch, L.; Höck, M.; Bertau, M. Lithium market research-global supply, future demand and price development. *Energy Storage Mater.* **2017**, *6*, 171−179.

(10) Liu, G.; Zhao, Z.; Ghahreman, A. Novel approaches for lithium extraction from salt-lake brines: A review. *Hydrometallurgy* **2019**, *187*, 81−100.

(11) Xu, X.; Chen, Y.; Wan, P.; Gasem, K.; Wang, K.; He, T.; Adidharma, H.; Fan, M. Extraction of lithium with functionalized lithium ion-sieves. *Prog. Mater. Sci.* **2016**, *84*, 276−313.

(12) Lai, X.; Xiong, P.; Zhong, H. Extraction of lithium from brines with high Mg/Li ratio by the crystallization-precipitation method. *Hydrometallurgy* **2020**, *192*, 105252.

(13) Ren, Z.; Wei, X.; Li, R.; Wang, W.; Wang, Y.; Zhou, Z. Highly selective extraction of lithium ions from salt lake brines with sodium tetraphenylborate as co-extractant. *Sep. Purif. Technol.* **2021**, *269*, 118756.

(14) Zhou, Z.; Fan, J.; Liu, X.; Hu, Y.; Wei, X.; Hu, Y.; Wang, W.; Ren, Z. Recovery of lithium from salt-lake brines using solvent extraction with TBP as extractant and $FeCl_3$ as co-extraction agent. *Hydrometallurgy* **2020**, *191*, 105244.

(15) Chen, X.; Ruan, X.; Kentish, S. E.; Li, G. K.; Xu, T.; Chen, G. Q. Production of lithium hydroxide by electrodialysis with bipolar membranes. *Sep. Purif. Technol.* **2021**, *274*, 119026.

(16) Nie, Z.; Bu, L.; Zheng, M.; Huang, W. Experimental study of natural brine solar ponds in Tibet. *Sol. Energy* **2011**, *85*, 1537−1542.

(17) Ding, T.; Zheng, M.; Nie, Z.; Ma, L.; Ye, C.; Wu, Q.; Zhao, Y.; Yang, D.; Wang, K. Impact of Regional Climate Change on the Development of Lithium Resources in Zabuye Salt Lake, Tibet. *Front. Earth Sci.* **2022**, *10*, 865158.

(18) Hong, H.-J.; Ryu, T.; Park, I.-S.; Kim, M.; Shin, J.; Kim, B.-G.; Chung, K.-S. Highly porous and surface-expanded spinel hydrogen manganese oxide (HMO)/Al_2O_3 composite for effective lithium (Li) recovery from seawater. *Chem. Eng. J.* **2018**, *337*, 455−461.

(19) Marthi, R.; Smith, Y. R. Selective recovery of lithium from the Great Salt Lake using lithium manganese oxide-diatomaceous earth composite. *Hydrometallurgy* **2019**, *186*, 115−125.

(20) Ding, T.; Wu, Q.; Zheng, M.; Nie, Z.; Li, M.; Peng, S.; Wang, Y.; Yu, X.; Qian, C.; Tang, S.; Wang, M. Polyacrylonitrile/Crown Ether Composite NanofibresWith High Efficiency for Adsorbing Li(I):Experiments and Theoretical Calculations. *Front. Energy Res.* **2021**, *9*, 765612.

(21) Chitrakar, R.; Kanoh, H.; Miyai, Y.; Ooi, K. Recovery of lithium from seawater using manganese oxide adsorbent ($H_{1.6}Mn_{1.6}O_4$) derived from $Li_{1.6}Mn_{1.6}O_4$. *Ind. Eng. Chem. Res.* **2001**, *40*, 2054−2058.

(22) Zhang, Q.-H.; Li, S.-P.; Sun, S.-Y.; Yin, X.-S.; Yu, J.-G. $LiMn_2O_4$ spinel direct synthesis and lithium ion selective adsorption. *Chem. Eng. Sci.* **2010**, *65*, 169−173.

(23) Zhang, G.; Zhang, J.; Zhou, Y.; Qi, G.; Zeng, J.; Sun, Y.; Shen, Y.; Li, X.; Ren, X.; Dong, S.; Sun, C.; Wu, Z.; Hai, C.; Tang, W. Practical synthesis of manganese oxide $MnO_2{\cdot}0.5H_2O$ for an advanced and applicable lithium ion-sieve. *J. Solid State Chem.* **2021**, *293*, 121768.

(24) He, G.; Zhang, L.; Zhou, D.; Zou, Y.; Wang, F. The optimal condition for H_2TiO_3 −lithium adsorbent preparation and Li^+ adsorption confirmed by an orthogonal test design. *Ionics* **2015**, *21*, 2219−2226.

(25) Gu, D.; Sun, W.; Han, G.; Cui, Q.; Wang, H. Lithium ion sieve synthesized via an improved solid state method and adsorption performance for West Taijinar Salt Lake brine. *Chem. Eng. J.* **2018**, *350*, 474−483.

(26) Moazeni, M.; Hajipour, H.; Askari, M.; Nusheh, M. Hydrothermal synthesis and characterization of titanium dioxide nanotubes as novel lithium adsorbents. *Mater. Res. Bull.* **2015**, *61*, 70−75.

(27) Wang, S.-L.; Lin, C.-H.; Yan, Y.-Y.; Wang, M. K. Synthesis of Li/Al LDH using aluminum and LiOH. *Appl. Clay Sci.* **2013**, *72*, 191−195.
(28) Qu, J.; He, X.; Wang, B.; Zhong, L.; Wan, L.; Li, X.; Song, S.; Zhang, Q. Synthesis of Li−Al layered double hydroxides via a mechanochemical route. *Appl. Clay Sci.* **2016**, *120*, 24−27.
(29) Cai, J.; Zhao, X.; Zhang, Y.; Zhang, Q.; Pan, B. Enhanced fluoride removal by Ladoped Li/Al layered double hydroxides. *J. Colloid Interface Sci.* **2018**, *509*, 353−359.
(30) Xiao, J.-L.; Sun, S.-Y.; Song, X.; Li, P.; Yu, J.-G. Lithium ion recovery from brine using granulated polyacrylamide−MnO_2 ion-sieve. *Chem. Eng. J.* **2015**, *279*, 659−666.
(31) Hong, H.-J.; Park, I.-S.; Ryu, J.; Ryu, T.; Kim, B.-G.; Chung, K.-S. Immobilizatiron of hydrogen manganese oxide (HMO) on alpha-alumina bead (AAB) to effective recovery of Li^+ from seawater. *Chem. Eng. J.* **2015**, *271*, 71−78.
(32) Ryu, T.; Shin, J.; Lee, D.-H.; Ryu, J.; Park, I.; Hong, H.; Kim, B.-G.; Lee, J. B.; Huh, Y. S.; Chung, K.-S. Improvement of lithium adsorption capacity of porous cylinder-type lithium manganese oxide through introduction of additive. *Mater. Chem. Phys.* **2015**, *167*, 225−230.
(33) Nisola, G. M.; Limjuco, L. A.; Vivas, E. L.; Lawagon, C. P.; Park, M. J.; Shon, H. K.; Mittal, N.; Nah, I. W.; Kim, H.; Chung, W.-J. Macroporous flexible polyvinyl alcohol lithium adsorbent foam composite prepared via surfactant blending and cryo-desiccation. *Chem. Eng. J.* **2015**, *280*, 536−548.
(34) Xiao, G.; Tong, K.; Zhou, L.; Xiao, J.; Sun, S.; Li, P.; Yu, J. Adsorption and desorption behavior of lithium ion in spherical PVC − MnO_2 ion sieve. *Ind. Eng. Chem. Res.* **2012**, *51*, 10921−10929.
(35) Sun, Y.; Guo, X.; Hu, S.; Xiang, X. Highly efficient extraction of lithium from salt lake brine by LiAl-layered double hydroxides as lithium-ion-selective capturing material. *J. Energy Chem.* **2019**, *34*, 80−87.
(36) Jiang, H.; Yang, Y.; Sun, S.; Yu, J. Adsorption of lithium ions on lithium-aluminum hydroxides: Equilibrium and kinetics. *Can. J. Chem. Eng.* **2020**, *98*, 544−555.
(37) Li, S.; Yue, X.; Jing, Y. Fabrication of zonal thiol-functionalized silica nanofibers for removal of heavy metal ions from wastewater. *Colloids Surf., A* **2011**, *380*, 229−233.
(38) Ji, Y.; Wen, Y.; Wang, Z.; Zhang, S.; Guo, M. Eco-friendly fabrication of a cost-effective cellulose nanofiber-based aerogel for multifunctional applications in Cu(II) and organic pollutants removal. *J. Cleaner Prod.* **2020**, *255*, 120276.
(39) Jamshidifard, S.; Koushkbaghi, S.; Hosseini, S.; Rezaei, S.; Karamipour, A.; Jafari rad, A.; Irani, M. Incorporation of UiO-66-NH2 MOF into the PAN/chitosan nanofibers for adsorption and membrane filtration of Pb (II), Cd (II) and Cr (VI) ions from aqueous solutions. *J. Hazard. Mater.* **2019**, *368*, 10−20.
(40) Koushkbaghi, S.; Zakialamdari, A.; Pishnamazi, M.; Ramandi, H. F. Aminated-Fe_3O_4 nanoparticles filled chitosan/PVA/PES dual layers nanofibrous membrane for the removal of Cr(VI) and Pb(II) ions from aqueous solutions in adsorption and membrane processes. *Chem. Eng. J.* **2018**, *337*, 169−182.
(41) Silbaugh, T. L.; Giorgi, J. B.; Ye, X. Adsorption Energy of tert-Butyl on Pt(III) by Dissociation of tert-Butyl Iodide: Calorimetry and DFT. *J. Phys. Chem. C* **2014**, *118*, 427−438.
(42) Hirata, A.; Kang, L. J.; Fujita, T.; Klumov, B.; Matsue, K.; Kotani, M.; Yavari, A. R.; Chen, M. W. Geometric Frustration of Icosahedron in Metallic Glasses. *Science* **2013**, *341*, 376−379.
(43) Al Zoubi, W.; Allaf, A. W.; Assfour, B.; Ko, Y. G. Toward two-dimensional hybrid organic-inorganic materials based on a I-PE/UHV-PVD system for exceptional corrosion protection. *Appl. Mater. Today* **2021**, *24*, 101142.
(44) Mahammedi, N. A.; Ferhat, M.; Tsumuraya, T. Prediction of optically-active transitions in type-VIII guest-free silicon clathrate Si46: A comparative study of its physical properties with type-I counterpart through first-principles. *J. Appl. Phys.* **2017**, *122*, 205103.
(45) Shang, S. L.; Wang, W. Y.; Zhou, B. C.; Wang, Y.; Darling, K. A.; Kecskes, L. J.; Mathaudhu, S. N.; Liu, Z. K. Generalized stacking fault energy, ideal strength and twinnability of dilute Mg-based alloys: A first-principles study of shear deformation. *Acta Mater.* **2014**, *67*, 168−180.
(46) Volzone, C.; Ortiga, J. SO_2 gas adsorption by modified kaolin clays: Influence of previous heating and time acid treatments. *J. Environ. Manage.* **2011**, *92*, 2590−2595.
(47) Britto, S.; Kamath, P. V. Structure of bayerite-based lithium-aluminum layered double hydroxides (LDHs): observation of monoclinic symmetry. *Inorg. Chem.* **2009**, *48*, 11646−11654.
(48) Chen, J.; Lin, S.; Yu, J. Quantitative effects of Fe_3O_4 nanoparticle content on Li^+ adsorption and magnetic recovery performances of magnetic lithium-aluminum layered double hydroxides in ultrahigh Mg/Li ratio brines. *J. Hazard. Mater.* **2020**, *388*, 122101.
(49) Hierso, J.; Sel, O.; Ringuede, A.; Laberty-Robert, C.; Bianchi, L.; Grosso, D.; Sanchez, C. Design, synthesis, structural and textural characterization, and electrical properties of mesoporous thin films made of rare earth oxide binaries. *Chem. Mater.* **2009**, *21*, 2184−2192.
(50) Al Zoubi, W.; Kamil, M. P.; Fatimah, S.; Nashrah, N.; Ko, Y. G. Recent advances in hybrid organic-inorganic materials with spatial architecture for state-of-the-art applications. *Prog. Mater. Sci.* **2020**, *112*, 100663.
(51) Li, Y.; Wang, Z.; Pan, Z.; Niu, X.; Yu, Y.; Meng, S. Pore structure and its fractal dimensions of transitional shale: A cross-section from east margin of the Ordos Basin, China. *Fuel* **2019**, *241*, 417−431.
(52) Sing, K. S. W. Reporting physisorption data for gas/solid systems with special reference to the determination of surface area and porosity. *Pure Appl. Chem.* **1985**, *57*, 603−619.
(53) Groen, J. C.; Peffer, L. A. A.; Pérez-RamıRez, J. Pore size determination in modified micro and mesoporous materials. Pitfalls and limitations in gas adsorption data analysis. *Microporous Mesoporous Mater.* **2003**, *60*, 1−17.
(54) Al Zoubi, W.; Allaf, A. W.; Assfour, B.; Ko, Y. G. Concurrent Oxidation−Reduction Reactions in a Single System Using a Low-Plasma Phenomenon: Excellent Catalytic Performance and Stability in the Hydrogenation Reaction. *ACS Appl. Mater. Interfaces* **2022**, *14*, 6740−6753.
(55) Zhong, J.; Lin, S.; Yu, J. Effects of Excessive Lithium Deintercalation on Li^+ Adsorption Performance and Structural Stability of Lithium/Aluminum Layered Double Hydroxides. *J. Colloid Interface Sci.* **2020**, *572*, 107.
(56) Alexander, M. R.; Thompson, G. E.; Beamson, G. Characterization of the oxide/hydroxide surface of aluminium using x-ray photoelectron spectroscopy: a procedure for curve fitting the O^{1s} core level. *Surf. Interface Anal.* **2000**, *29*, 468−477.
(57) Alba, M. D.; Alvero, R.; Becerro, A. I.; Castro, M. A.; Trillo, J. M. Chemical Behavior of Lithium Ions in Reexpanded Li−Montmorillonites. *J. Phys. Chem. B* **1998**, *102*, 2207−2213.
(58) Zhong, J.; Lin, S.; Yu, J. Lithium recovery from ultrahigh Mg^{2+}/Li^+ ratio brine using a novel granulated Li/Al-LDHs adsorbent. *Sep. Purif. Technol.* **2021**, *256*, 117780.
(59) Zheng, Y.; Cheng, B.; Fan, J.; Yu, J.; Ho, W. Review on nickel-based adsorption materials for Congo red. *J. Hazard. Mater.* **2021**, *403*, 123559.
(60) Isupov, V. P.; Kotsupalo, N. P.; Nemudry, A. P.; Menzeres, L. T. Aluminium hydroxide as selective sorbent of lithium salts from brines and technical solutions. *Stud. Surf. Sci. Catal.* **1999**, *120*, 621−652.
(61) Meng, Q.; Qin, K.; Ma, L.; He, C.; Liu, E.; He, F.; Shi, C.; Li, Q.; Li, J.; Zhao, N. N-doped porous carbon nanofibers/porous silver network hybrid for high-rate supercapacitor electrode. *ACS Appl. Mater. Interfaces* **2017**, *9*, 30832−30839.

https://doi.org/10.1021/acsomega.2c00658
ACS Omega 2022, 7, 11430−11439